

MEMBRANES

Aromatic-aliphatic hydrocarbon separation with oriented monolayer polyhedral membrane

Hao Sun¹, Naixin Wang^{1*}, Yinghui Xu¹, Fengkai Wang¹, Jun Lu², Huanting Wang², Quan-Fu An^{1*}

Aromatic-aliphatic hydrocarbon separation is a challenging but important industrial process. Pervaporation membrane technology has the potential for separating these mixtures. We developed an oriented monolayer polyhedral (OMP) membrane that consists of a monolayer of ordered polyhedral particles and is anchored by hyperbranched polymers. It contains a high density of straight, selective nanochannels, enabling the preferential transport of aromatic molecules. Compared with traditional mixed-matrix membranes with random orientations, the OMP membrane improves the pervaporation separation index for aromatic-aliphatic hydrocarbon mixtures with C₆ and C₇ compounds, surpassing the performance of existing membranes by 3 to 10 times. This high performance demonstrates the potential of OMP membranes for hydrocarbon molecular separation and their application in the value-added separation of naphtha feedstocks.

Light olefins such as ethylene are crucial petrochemical products, with global production reaching hundreds of millions of tons annually (1). Naphtha steam cracking is used to produce >50% of light olefins. However, the cracking process is the most energy-intensive single process in the petrochemical industry (2, 3). Aromatics in naphtha that cannot participate in the cracking reaction coke the furnace and reduce the yield and increase costs (4). “Molecular refining” offers an approach for maximizing the value of all feed molecules. By reconstructing the components of naphtha, separating aromatic and aliphatic hydrocarbons, ideal steam-cracking feedstock and high value-added aromatic hydrocarbon product feedstock can be obtained. Adsorption methods, including simulated moving beds, have been reported to be effective for aromatic-aliphatic separations from multicomponent model mixtures (5, 6). As an alternative technique, pervaporation membrane technology has also demonstrated potential in liquid-phase molecular separation because of its low energy consumption, high efficiency, and feasible integration into other processes (7, 8). This provides theoretical possibility for the efficient separation of aromatic-aliphatic hydrocarbons in naphtha.

However, separating aromatic-aliphatic hydrocarbons is challenging because of their similar physicochemical properties and easy azeotropes (9–13). They have similar kinetic diameters and entangling molecular configurations, so the size-sieving effect cannot ensure precise separation of these two types of molecules (14). Most studies on aromatic-aliphatic hydrocarbon pervaporation are based

on aromatic-friendly polymer membranes. These membranes rely on the polarization of aromatic molecules with delocalized π electrons induced by polar functional groups, resulting in different diffusion behaviors of aromatic and aliphatic molecules in the membrane, thereby achieving separation (15, 16). However, the disordered cross-linked network structure of polymer membranes has tortuous nanochannels with a relatively large pore size distribution, which inhibits improvements in the permeability and selectivity (17–19). The performance of mixed-matrix membranes, which are based on porous crystal materials with a regular polyhedral morphology, can be improved by creating multiple low-resistance selective transport channels within the membrane (20–23). Unfortunately, because of the low loading and disordered agglomeration of fillers, high-performance transport paths are often blocked by multisegment polymer matrices (24–26). Optimizing the spatial arrangement of crystal particles can create well-defined paths that enhance rapid and selective molecular transport (27–29). Building on this understanding, our approach aims to fully and rationally use the structural characteristics of regular polyhedrons of porous crystal materials to construct ordered, densely distributed, and interconnected selective molecular transport channels.

We present a step-by-step spin-coating method for creating oriented monolayer polyhedral (OMP) membranes using metal-organic framework (MOF) materials. MOF particles with a regular octahedral structure were assembled on the porous substrate, after which the gaps between particles were sealed with a polymer. These membranes feature interconnected straight channels and are ideal for the ultrafast separation of aromatic-aliphatic hydrocarbons through pervaporation (Fig. 1A and fig. S1). The OMP membrane contains a high-density distribution of oriented monolayer MOF particles, providing rapid and selective channels that

dominate the molecular transport process. The polymer anchoring the MOF phase endows the membrane with excellent flexibility and durability. As a proof of concept, we designed a two-stage cascade separation process to demonstrate the high stability of the OMP membrane for hydrocarbon separation in the naphtha system.

Rational design of the OMP membrane

We selected UiO-66 (30), a well-known type of MOF, as the primary material for the membrane. UiO-66 has a stable pore structure and a large porosity that allows for efficient molecular transport. Additionally, its window aperture size is ~0.6 nm, which ensures the smooth passage of both aromatic and aliphatic molecules (0.43 to 0.6 nm) (fig. S2 and table S1). UiO-66, with its regular octahedral morphology, typically exists on a flat substrate surface in the most thermodynamically stable state. This means that its triangular planes will attach to the substrate surface, resulting in a (111) plane orientation. This orientation ensures that the pores of UiO-66 are nearly perpendicular to the membrane surface, facilitating efficient motion between the molecular diffusion path in the membrane and the substrate pore (Fig. 1A). Therefore, our initial objective was to construct a high-density monolayer MOF through a spin-coating process. To understand the monolayer arrangement of MOF particles formed by MOF dispersion under shear stress induction, we determined that the high-density monolayer MOF layer is influenced mainly by the particle properties (size and uniformity), process conditions (spin-coating speed), and dispersion (concentration and stability) (Fig. 1B).

Acetic acid was used as a modulator to adjust the properties of the MOF particles because it will (i) modulate and synthesize monodisperse regular octahedral crystal particles of uniform size and (ii) introduce lattice defects to the MOF, particularly missing-linker defects, which can create nonfully coordinated Zr-O clusters serving as adsorption sites for specific hydrocarbon molecules. As the concentration of acetic acid increased from 0 M to 4.8 M, there was a significant reduction in the agglomeration of MOF particles, leading to a more uniform octahedral morphology (figs. S3 and S4). To obtain a highly oriented and thinner MOF layer, it is important to ensure that the UiO-66 particles have a distinct octahedral morphology while being as small as possible. In this study, UiO-66 particles with an acetic acid concentration of 2.4 M and an average size of 760 nm were deemed optimal. The orientation structure suffers if the particles are too small, as evidenced by the much lower orientation of the UiO-66 particles after a reaction time of 10 hours compared with those after 24 hours (fig. S5). This highlights the importance of a regular octahedral morphology in the formation of the orientation structure.

¹Beijing Key Laboratory for Green Catalysis and Separation, Department of Chemical Engineering, College of Materials Science and Engineering, Beijing University of Technology, Beijing, China. ²Department of Chemical and Biological Engineering, Monash University, Victoria, Australia.

*Corresponding author. Email: wangnx@bjut.edu.cn (N.W.); anqf@bjut.edu.cn (Q.-F.A.)

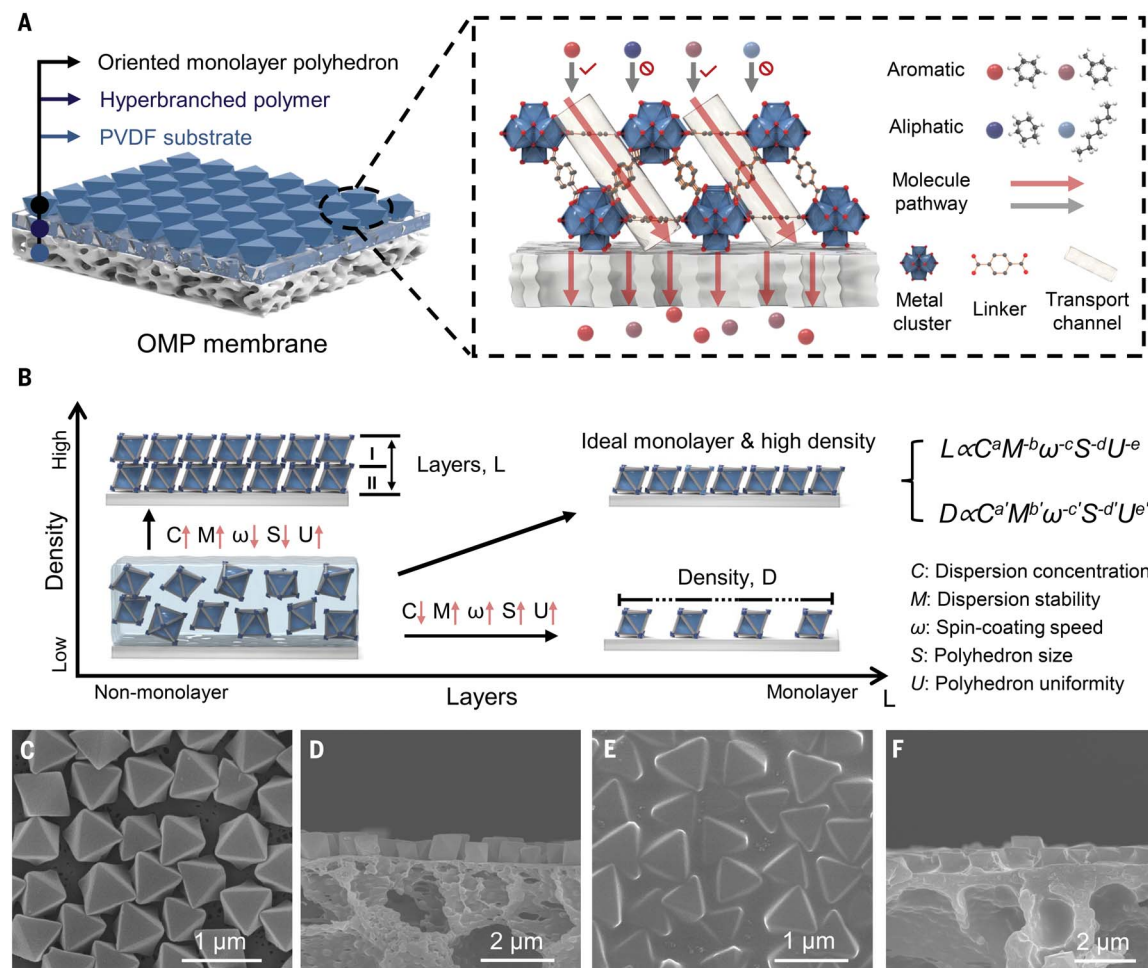


Fig. 1. Design of the OMP membrane. (A) Schematic of the structure and selective molecular transport of OMP membranes in which aromatic molecules selectively pass through the ordered interconnected straight channels in the polyhedron. (B) High-density monolayer polyhedral construction strategy. (C to F) Surface and cross-sectional SEM images of the oriented monolayer polyhedron layer [(C) and (D)] and the OMP membrane [(E) and (F)].

In the spin-coating process, gravity causes the UiO-66 particles to settle after coating the substrate surface. Simultaneously, the shear force parallel to the substrate direction from the spin-coating process can effectively prevent the accumulation of UiO-66 particles as a multi-layer, resulting in a monolayer distribution. Because they are in the thermodynamically most stable state, the particles tend to exhibit the (111) plane orientation (fig. S6). We used the crystallographic preferred orientation index to assess the degree of orientation (37). By adjusting the spin-coating speed and drying temperature (fig. S7), we obtained monolayer UiO-66 with a high orientation of the (111) plane under optimal preparation conditions, achieving a crystallographic preferred orientation index of 59.7 (figs. S8 to S10).

To obtain an intact and continuous OMP membrane, the MOF layer needs to be anchored and filled with nonselective defects between MOF crystals. On the basis of our previous research (32, 33), we chose hyperbranched polymers (HBPs)

as potential candidates because of their higher aromatic selectivity and flux (figs. S11 to S13). The low viscosity (3.8 mPa s) of the HBP enables it to sink downward during the spin-coating process, effectively sealing gaps between MOF particles tens of nanometers in size rather than forming a thick layer on the surface of the oriented MOF layer. As a result, the anchoring of MOF particles and the precise repair of defects can be achieved without significantly affecting the orientation of the MOF layer (Fig. 1, C to F, and fig. S14). Grazing incidence wide-angle X-ray scattering (GIWAXS), two-dimensional (2D) XRD, and pole figure XRD further confirmed the high (111) orientation of the OMP membrane (figs. S15 and S16). The AFM results revealed that the introduction of MOF particles significantly increased the roughness of the membrane (figs. S17 and S18A). When the polymer fills the UiO-66 crystal gap, the height of the polymer surface is slightly lower than that of the UiO-66 particles, with a difference of ~380 nm (fig. S18B). This structure exposes UiO-66 par-

ticles to the membrane surface as much as possible, thereby maximizing the performance of the MOF.

In our strategy, achieving high-density selective molecular transport channels relies on the high coverage of MOFs. We studied the impact of different MOF dispersion concentrations on OMP membranes. A toluene-*n*-heptane mixture was used as a probe system to evaluate the separation performance of the OMP membrane. As shown in Fig. 2A, before reaching the optimal loading (concentration of 4 g/liter), as the concentration of the MOF dispersion increased, the arrangement of the MOF particles tended to become closer (fig. S19), the coverage area gradually increased (Fig. 2B and figs. S20 and S21), and the selectivity and permeability improved simultaneously. When the concentration of the dispersion exceeded 4 g/liter, the flux decreased sharply. At this time, because the arrangement of the MOF particles is already close enough, the coverage rate does not significantly improve but leads to nonmonolayer

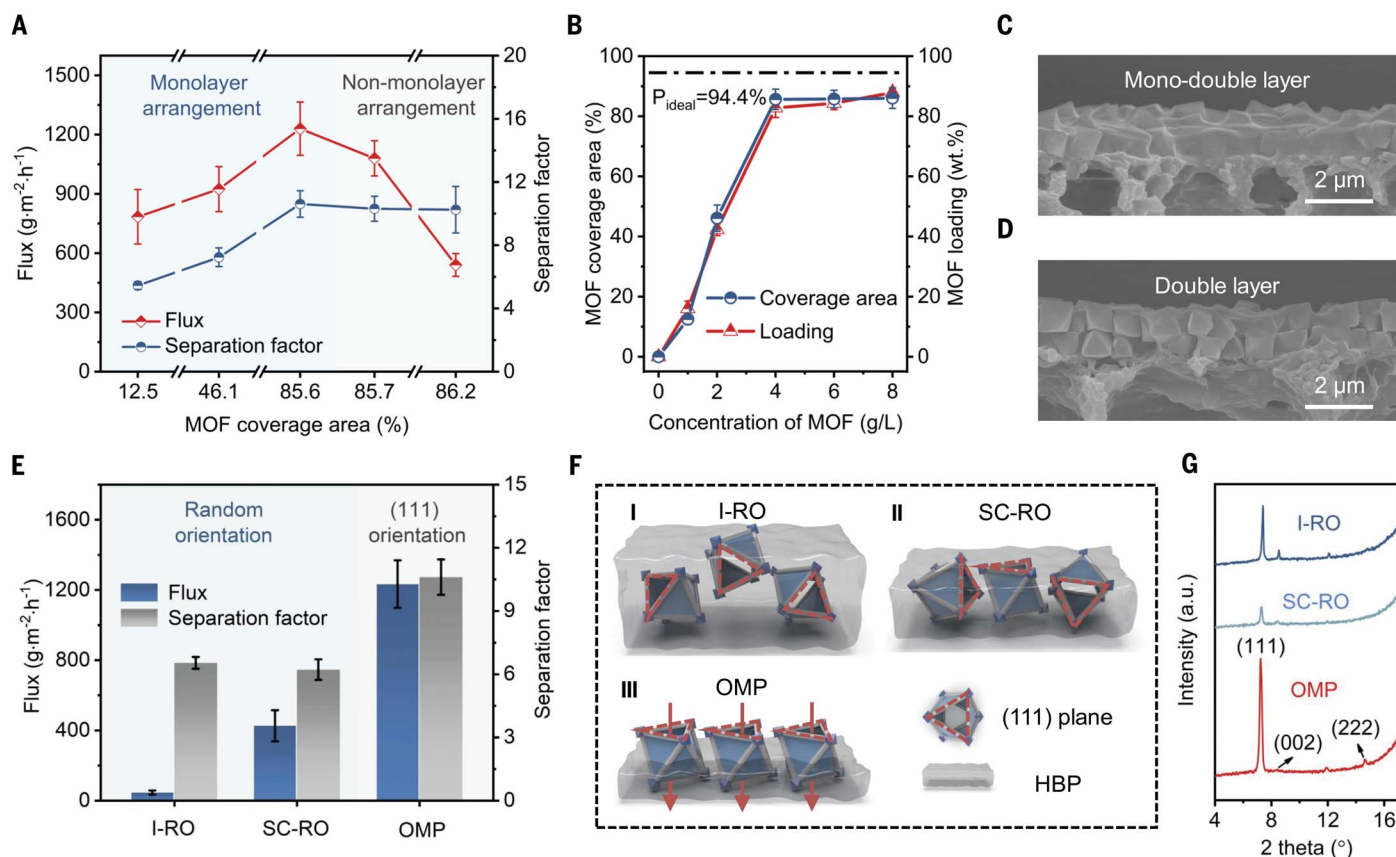


Fig. 2. Regulation of the OMP membrane structure. (A) Effect of the percentage of MOF area on the separation performance (50 wt % toluene and 50 wt % *n*-heptane mixtures at 40°C). Error bars represent the SDs based on three independent tests. (B) Percentage of the MOF area and loading at different dispersion concentrations. The MOF area on the top view of the membrane surface was calculated using ImageJ in combination with SEM images. Error bars represent the SDs based on three independent measurements. (C and D) Cross-sectional SEM images of the membranes prepared

with different MOF dispersion concentrations: 6 g/liter (C) and 8 g/liter (D). (E) Separation performance of randomly oriented and (111)-oriented MOF membranes (50 wt % toluene and 50 wt % *n*-heptane mixtures at 40°C). Error bars represent the SDs based on three independent tests. (F) Schematic illustration of MOF states in OMP membranes and randomly oriented membranes. Pore windows for molecular penetration are represented by red triangles. (G) X-ray diffraction patterns of randomly oriented and (111)-oriented MOF membranes.

accumulation of MOF particles, resulting in a significant increase in the mass transfer distance (Fig. 2, C and D). At the optimal concentration, the MOF coverage reached 85.6% (with an MOF mass loading of 82.8%), which is close to the 94.4% coverage achieved by an optimized arrangement under ideal conditions (fig. S22). Furthermore, compared with the pure HBP membrane, the OMP membrane achieved improved flux and separation factors simultaneously (fig. S23), indicating a better comprehensive performance.

We further compared the separation performance differences between the OMP membranes and randomly oriented membranes obtained through the blend immersion (I-RO) and direct blend spin-coating methods (SC-RO) (Fig. 2E). In the I-RO and SC-RO membranes, MOF particles are randomly oriented and completely wrapped by polymers, resulting in molecules having to travel through long transport paths and multiple low-selectivity regions (Fig. 2,

F and G, and fig. S24). Compared with that of randomly oriented membranes, the permeability of the OMP membrane significantly improved, and the separation factor increased by 62.2 and 70.6%, respectively.

Molecular transport mechanism

To understand the selective transport mechanism of aromatic hydrocarbon molecules in membranes, we chose two other MOF materials, ZIF-67 and Cu-BTC, and prepared MOF@HBP membranes with similar structures using the same method (figs. S25 and S26). The empty electron orbitals of the transition metals in ZIF-67 (Co^{2+}) and Cu-BTC (Cu^{2+}) can form complexes with the π electrons of aromatic compounds, giving them a certain capacity for adsorbing aromatics (15, 34). Despite the similar particle sizes of the three MOFs, there are significant differences in the separation performances of the three membranes (fig. S27). The pore size of ZIF-67 (0.34 nm) is much smaller

than the kinetic diameter of toluene or *n*-heptane molecules, resulting in a low flux of $209 \text{ g m}^{-2} \text{ h}^{-1}$ for the ZIF-67@HBP membrane, which is even lower than that of the pure HBP membrane (fig. S28). Conversely, the Cu-BTC@HBP membrane has the highest flux due to its larger pore size (0.9 nm), but its separation factor is only 6.7. By comparison, the appropriate pore size of UiO-66 facilitated the selective transport of toluene molecules.

We further used characterization and molecular simulations to explain the efficient separation of aromatic-aliphatic mixtures by the OMP membrane. Low-field nuclear magnetic resonance was used to detect the transverse relaxation time (T_2) of the hydrogen protons in the liquid molecules of the membrane pores. This provides information about the void size in membrane pores or the presence of solvent molecules (35, 36). The peak value of the low relaxation time (0.1 to 200 ms) represents the strength of the adsorption capacity of the

solvent in the confined space of the nanometer and subnanometer ranges. The T_2 relaxation time signal in both regions corresponds to two different states of solvent molecules in the membrane: molecules in MOF regular pores (0.1 to 10 ms) and molecules in the HBP free volume (10 to 200 ms) (fig. S29). The results are shown in Fig. 3A. Compared with the HBP membrane, the OMP membrane exhibited prominent preferential adsorption of toluene. In addition, we used benzene-cyclohexane and toluene-*n*-heptane with six and seven carbon atoms, respectively, as probe molecules to test the difference in vapor adsorption of UiO-66. This finding indicates that UiO-66 has stronger adsorption for aromatic molecules (Fig. 3B).

In the framework of UiO-66, the benzene ring, Zr-O cluster, and missing-linker defects can act as preferred adsorption sites for aromatic molecules (Fig. 3C). Density functional theory was used to evaluate the adsorption energy of aromatic molecules at various adsorption sites in UiO-66 (fig. S30). The findings indicate that the binding energy of benzene with toluene in UiO-66 is $57.9 \text{ kcal mol}^{-1}$, which is significantly greater than that with *n*-heptane ($7.15 \text{ kcal mol}^{-1}$) (Fig. 3E). This is primarily attributed to the π - π interactions between benzene rings. In addition, the defect site and the Zr-OH cluster also exhibit strong binding energies for toluene. On the basis of the thermogravimetric analysis results, the ligand deletion ratio of UiO-66 syn-

thesized under optimal conditions was ~13.6% (fig. S31) (37). The exposed defect sites can serve as effective aromatic adsorption sites (10). Further investigation of the molecular transport behavior of organic molecules in UiO-66 and HBP was performed using a probe mixture of toluene and *n*-heptane (Fig. 3D and figs. S32 and S33). The simulation results indicate that the number of toluene molecules entering the permeation chamber through the (111)-oriented UiO-66 membrane is 1.71 times greater than the number of *n*-heptane molecules entering the permeation chamber within 400 ps (Fig. 3F). Conversely, under the same conditions, it was difficult for toluene and *n*-heptane molecules to permeate through the pure HBP membrane,

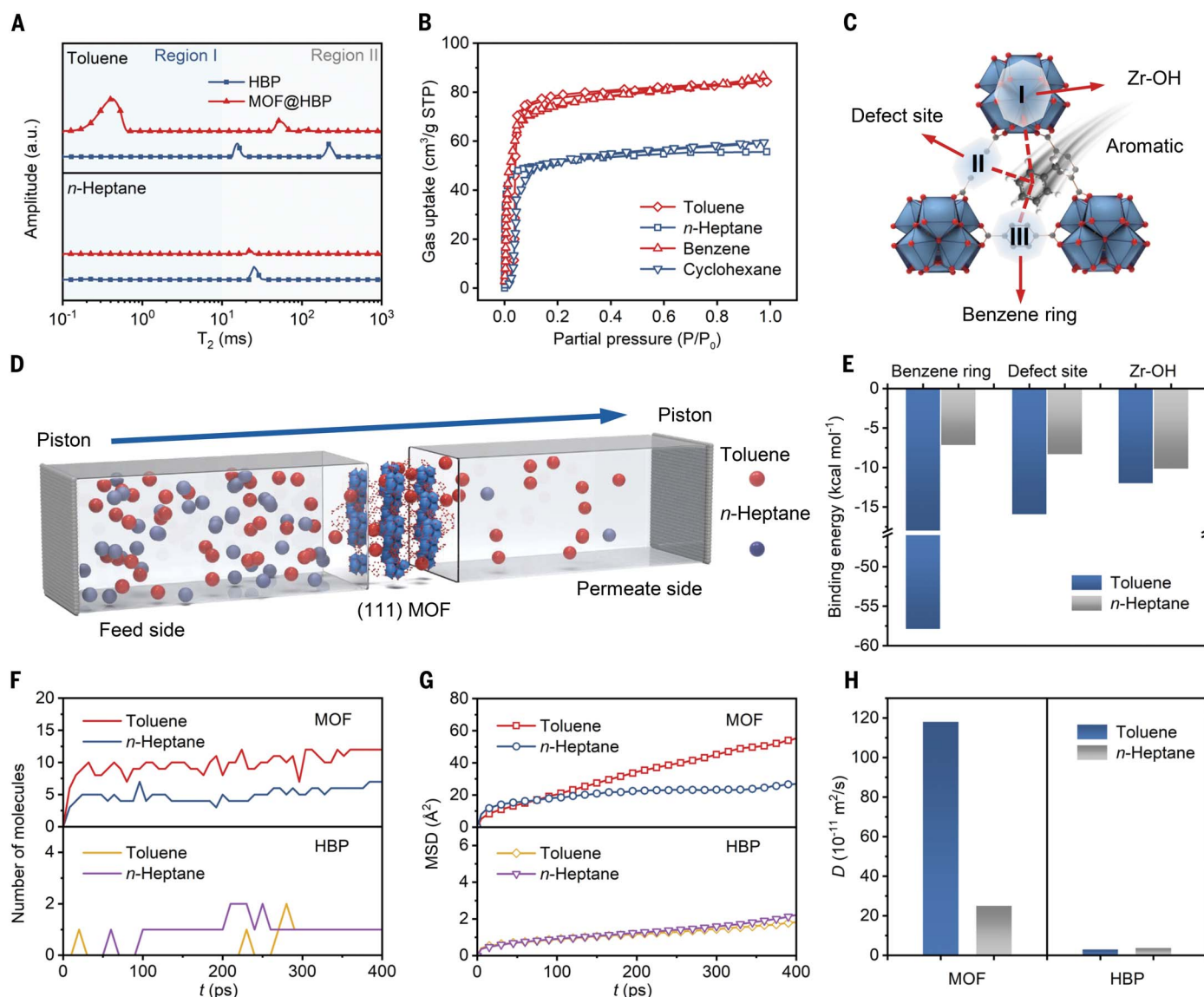


Fig. 3. Molecular selective transport mechanism. (A) Proton transverse relaxation time T_2 distributions of toluene and *n*-heptane in different membranes. (B) Toluene, *n*-heptane, benzene, and cyclohexane adsorption isotherms. (C) Possible aromatic adsorption sites in the MOF structure. (D) Schematic of the molecular dynamics simulation. (E) Binding energies

of toluene and *n*-heptane for different MOF adsorption sites. (F) Number of toluene and *n*-heptane molecules permeating through the MOF and HBP membranes as a function of time. (G) MSD curves of toluene and *n*-heptane in MOF and HBP. (H) Self-diffusion coefficient D of toluene and *n*-heptane in the MOF and HBP.

with only 3.3% (one in 30) of the molecules successfully permeating. The diffusion coefficients of toluene and *n*-heptane were calculated by fitting the mean square displacement (MSD) results (Fig. 3, G and H). The diffusion coefficient of toluene in UiO-66 was ~4.7 times greater than that of *n*-heptane. These molecular dynamics simulation results confirm that the excellent separation properties of the MOF membrane derive from the oriented MOF channels.

Aromatic-aliphatic hydrocarbon separation performance

The impacts of different operating conditions, such as the feed temperature and toluene content, on the separation performance of the OMP

membranes were investigated (figs. S34 and S35). For a mixture of 50 wt % toluene and 50 wt % *n*-heptane at a lower operating temperature of 40°C, the membrane showed high permeability flux (1230 g m⁻² h⁻¹) and maintained high selectivity ($\alpha = 10.6$). Encouraged by these results, the separation performance of the membrane was further tested for other aromatic-aliphatic hydrocarbon mixtures, including benzene-cyclohexane, toluene-methylcyclohexane, and toluene-iso-octane (fig. S36). Compared with those of *n*-heptane, the larger molecular sizes of cyclohexane, methylcyclohexane, and iso-octane (table S1) led to improved aromatic selectivity for these mixtures. The separation factor for the toluene-iso-octane mixture reached 18.4.

In the chemical industry, it is crucial to separate aromatic and aliphatic hydrocarbons in naphtha to improve product quality and reduce production costs. Naphtha, consisting mainly of normal alkanes, isomeric alkanes, cycloalkanes, and aromatics with a carbon number range of C₅ to C₁₂, contains a relatively high proportion of C₆ to C₈ components. As a result, we selected four typical solvent molecules (normal heptane, isooctane, methylcyclohexane, and toluene) as the model naphtha feedstock. We designed a two-stage membrane cascade process to extract aromatic hydrocarbons from a mixture (Fig. 4A). As shown in Fig. 4B, after the two-stage membrane treatment, the aromatic content increased from 15 to 97.5 wt %, making it an ideal feedstock for high value-added

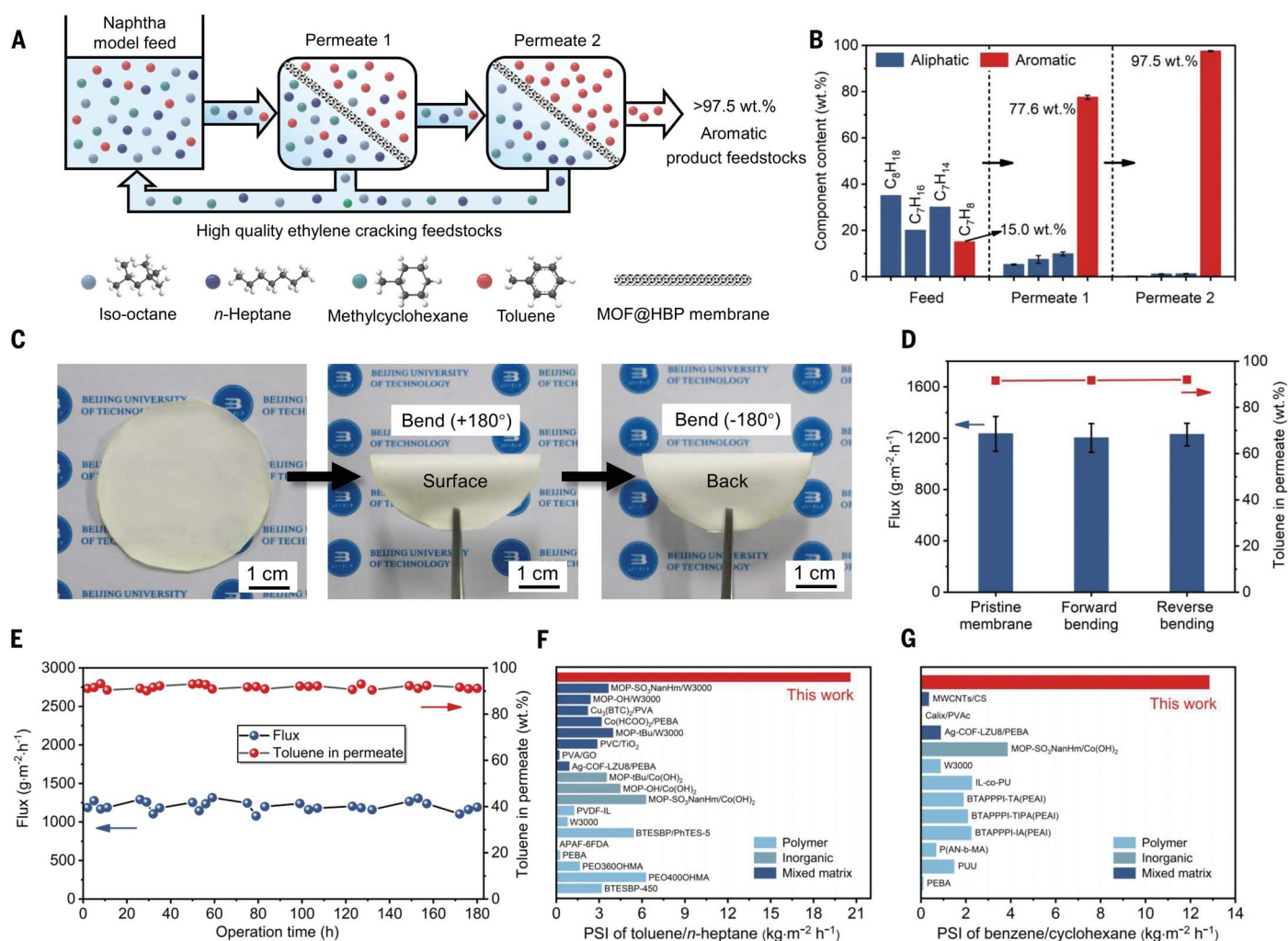


Fig. 4. Evaluation of the separation performance of the model naphtha system and membrane durability. (A) Schematic demonstration of the separation of aromatic and aliphatic hydrocarbons in a naphtha model feed through a two-stage membrane cascade process. (B) Separation performance of the OMP membranes for the naphtha model feed (35 wt % iso-octane, 20 wt % *n*-heptane, 30 wt % methylcyclohexane, and 15 wt % toluene mixtures at 40°C). Error bars represent the SDs based on three independent tests.

(C and D) Bending resistance test of the OMP membrane. Error bars represent the SDs based on three independent tests. (E) Long-term separation performance of the OMP membrane (50 wt % toluene and 50 wt % *n*-heptane mixtures at 40°C). (F and G) Separation performance of the OMP membrane compared with that of other state-of-the-art membranes. For pervaporation separation index (PSI) and other details, see the supplementary materials and tables S2 and S3.

aromatic products. The remaining aliphatic hydrocarbons can be used as high-quality ethylene-cracking feedstocks.

In practical applications, the bending resistance and stability of a membrane are key indicators of its usability. The interconnected structure of the polymer and MOF particles in the OMP membrane imparts excellent durability. The nanoscratch test results revealed that the adhesion strength (bonding force) between the separation layer and the support in the OMP membrane did not change significantly compared with that in the HBP membrane (fig. S37). Correspondingly, the OMP membrane exhibited minimal alterations in its microstructure and separation performance after undergoing 180° forward and backward bending (Fig. 4, C and D, and fig. S38). The operational stability and swelling resistance of the membrane are also crucial factors for practical applications. After a 72-hour swelling test, the mass change of the OMP membrane was the lowest (only 0.5%) compared with that of the polyvinylidene difluoride substrate and HBP membrane (fig. S39). Additionally, in the 180-hour cross-flow test, the performance of the OMP membrane was stably maintained, demonstrating its operating stability and swelling resistance (Fig. 4E). Compared with other state-of-the-art aromatic-aliphatic hydrocarbon separation membranes, the OMP membrane exhibited outstanding separation performance (Fig. 4, F and G).

Conclusions

We achieved high-performance separation of aromatic and aliphatic hydrocarbons in naphtha by creating a well-organized MOF monolayer membrane with interconnected straight channels. The MOF exhibited high

adsorption selectivity, allowing for the preferential adsorption of aromatic molecules. The oriented, interconnected, and high-density distribution of molecular transport channels in the monolayer MOF membrane ensured rapid molecular diffusion. Additionally, the use of a polymer helped to anchor the MOF crystal particles while repairing nonselective defects between particles, resulting in a membrane with excellent flexibility and durability. This work highlights the potential of membrane technology for separating complex liquid-phase hydrocarbon mixtures and demonstrates a strategy for designing membranes that offer superior performance in molecular separation.

REFERENCES AND NOTES

1. D. S. Sholl, R. P. Lively, *Nature* **532**, 435–437 (2016).
2. M. Yan, Y. Wang, J. Chen, J. Zhou, *Chem. Soc. Rev.* **52**, 6075–6119 (2023).
3. X. Sun, J. Chen, T. Ritter, *Nat. Chem.* **10**, 1229–1233 (2018).
4. S. Najari et al., *Chem. Soc. Rev.* **50**, 4564–4605 (2021).
5. S. Yang et al., *AIChE J.* **67**, e17375 (2021).
6. S. Guo et al., *Separ. Purif. Tech.* **215**, 410–421 (2019).
7. L. H. Xu et al., *Science* **378**, 308–313 (2022).
8. L. Jiang, Y. Wang, T. Chung, X. Qiao, J. Lai, *Prog. Polym. Sci.* **34**, 1135–1160 (2009).
9. L. Yang et al., *Chem. Soc. Rev.* **49**, 5359–5406 (2020).
10. Y. Han et al., *Chem* **9**, 739–754 (2023).
11. J. Zhou, G. Yu, Q. Li, M. Wang, F. Huang, *J. Am. Chem. Soc.* **142**, 2228–2232 (2020).
12. H. Yao et al., *Angew. Chem. Int. Ed.* **59**, 19945–19950 (2020).
13. W. G. Cui, T. L. Hu, X. H. Bu, *Adv. Mater.* **32**, e1806445 (2020).
14. J. R. Li, R. J. Kuppler, H. C. Zhou, *Chem. Soc. Rev.* **38**, 1477–1504 (2009).
15. L. Zhang et al., *J. Membr. Sci.* **598**, 117652 (2020).
16. C. P. Ribeiro Jr., B. D. Freeman, D. S. Kalika, S. Kalakkunnath, *Ind. Eng. Chem. Res.* **52**, 8906–8916 (2013).
17. J. Shen et al., *Nat. Mater.* **21**, 1183–1190 (2022).
18. J. Kloos et al., *Chem. Mater.* **33**, 8323–8333 (2021).
19. W. Yong, H. Zhang, *Prog. Mater. Sci.* **116**, 100713 (2021).
20. S. J. Datta et al., *Science* **376**, 1080–1087 (2022).
21. G. Chen et al., *Science* **381**, 1350–1356 (2023).
22. R. Freund et al., *Angew. Chem. Int. Ed.* **60**, 23975–24001 (2021).
23. S. Sorribas, P. Gorgojo, C. Téllez, J. Coronas, A. G. Livingston, *J. Am. Chem. Soc.* **135**, 15201–15208 (2013).

24. C. Li et al., *Sci. Adv.* **9**, eadf5087 (2023).
25. G. Liu et al., *Nat. Mater.* **17**, 283–289 (2018).
26. X. Ma, X. Wu, J. Caro, A. Huang, *Angew. Chem. Int. Ed.* **58**, 16156–16160 (2019).
27. T. C. T. Pham, H. S. Kim, K. B. Yoon, *Science* **334**, 1533–1538 (2011).
28. Z. Lai et al., *Science* **300**, 456–460 (2003).
29. D. Kim, M. Y. Jeon, B. L. Stottrup, M. Tsapatsis, *Angew. Chem. Int. Ed.* **57**, 480–485 (2018).
30. J. H. Cavka et al., *J. Am. Chem. Soc.* **130**, 13850–13851 (2008).
31. R. Wei et al., *Sci. Adv.* **8**, eabm6741 (2022).
32. Y. Zhang et al., *J. Membr. Sci.* **489**, 144–152 (2015).
33. N. Wang, S. Ji, J. Li, R. Zhang, G. Zhang, *J. Membr. Sci.* **455**, 113–120 (2014).
34. J. Du et al., *J. Membr. Sci.* **683**, 121840 (2023).
35. H. Sun et al., *Angew. Chem. Int. Ed.* **62**, e202300262 (2023).
36. W. H. Zhang et al., *Nat. Nanotechnol.* **16**, 337–343 (2021).
37. X. Wang et al., *Nat. Commun.* **13**, 266 (2022).

ACKNOWLEDGMENTS

We thank Z. Zhang (Petrochemical Research Institute, CNPC) for valuable discussions. H. Sun acknowledges Monash University for hosting his visiting research. J. Lu acknowledges the support provided by the ARC DECRA project (DE230100407). **Funding:** This work was supported by the National Natural Science Foundation of China (grants 22125801 and 22478012). **Author contributions:** Conceptualization: H.S., N.W., Q.-F.A.; Funding acquisition: N.W., Q.-F.A.; Investigation: H.S., Y.X., F.W., N.W.; Methodology: H.S., Y.X., F.W., N.W.; Project administration: N.W., Q.-F.A. Supervision: N.W., H.W., Q.A. Writing – original draft: H.S. Writing – review & editing: N.W., J.L., H.W., Q.-F.A. **Competing interests:** Chinese patents (application no. 202310792134.0) that cover the OMP membrane reported herein were filed by Beijing University of Technology. The authors declare no competing interests. **Data and materials availability:** All data are available in the main text or the supplementary materials. **License information:** Copyright © 2024 the authors, some rights reserved; exclusive licensee American Association for the Advancement of Science. No claim to original US government works. <https://www.science.org/about/science-licenses-journal-article-reuse>

SUPPLEMENTARY MATERIALS

science.org/doi/10.1126/science.adq5577
Materials and Methods
Figs. S1 to S40
Tables S1 to S3
References (38–60)

Submitted 21 May 2024; accepted 30 October 2024
10.1126/science.adq5577